SNR-based Denoising Dynamic Statistical Threshold Detection of FBG Spectral Peaks

Gabriel Cibira, Ivan Glesk, and Jozef Dubovan,

Abstract—This paper targets a Denoising Dynamic Statistical Threshold (DDST) detection algorithm of Fiber Bragg Grating (FBG) spectral peaks at the presence of changing Signal-to-Noise Ratio (SNR) in a sensing channel. Computing the DDST is based on statistical parameters of the background noise. The DDST is determined by adjusting it using the SNR via determining the targeted probability of false alarms (p_{FA}). The proposed algorithm implements background noise fluctuations, nonlinear signal attenuation of a Single-Mode Fiber (SMF), as well as influence of the short-term interference. The implemented sliding wavelength window technique in conjunction with the FBG spectral peaks power scaling allow automatic adjusting of p_{FA} and the DDST. During the possible FBGs resonant wavelengths overlap resulting from approaching/colliding spectral power responses of FBGs, the proposed algorithm also improves the detection robustness and resolving of these overlaps. The DDST marginally takes into account spectral shapes of FBGs resonant wavelength peaks. Advantageously, DDST wavelength resolving is independent of FBG spectral peaks shapes. Our DDST algorithm is also simple to implement. Measurements done by two Optical Spectral Analyzers (OSAs) confirmed significant improvements in the background noise reduction (i.e. signal denoising), noisy FBG spectral peaks shapes smoothing and SNR, improved adjacent FBG spectral peaks detectability and resolving. Our experiments also confirmed usability of the DDST algorithm under severe network conditions (with low reflected FBG power below -75 dB and low $SNR < 4$ dB resulting a standard deviation of $\sigma > 7$ dB in the background noise fluctuations).

Index Terms—Fiber Bragg grating sensors, denoising, dynamic statistical threshold, statistical detection, signal-to-noise ratio.

I. Introduction

FIBER Bragg Grating (FBG) construction and operating principles have been described in [1], [2], [3]. An FBG is a type of distributed optical structure longitudinally implemented into a short segment of optical fiber. Its internal

Gabriel Cibira is with Institute of Aurel Stodola, Faculty of Electrical Engineering and Information Technology, University of Zilina, Univerzitna 1, 01026 Zilina, Slovakia (e-mail: gabriel.cibira@uniza.sk).

Ivan Glesk is with the Electronic and Electrical Engineering Department, University of Strathclyde, Royal College Building, 204 George St, Glasgow, G11XW, United Kingdom (e-mail: ivan.glesk@strath.ac.uk).

Jozef Dubovan is with Department of Multimedia and Information-Communication Technologies, Faculty of Electrical Engineering and Information Technology, University of Zilina, Univerzitna 1, 01026 Zilina, Slovakia (e-mail: jozef.dubovan@uniza.sk).

structure determines specific bandwidth through which the resonant wavelength is reflected, while other wavelengths are transmitted. An FBG can therefore be used in telecommunications or intrinsic sensing applications as an inline optical filter (to block certain wavelengths), or as a wavelength-specific reflector [4]. Extrinsic sensing applications can use a fiber-integrated sensitive thin film as a sensor/transducer of environmental parameters [5]. The principle of temperature or strain FBG sensing is based on the fact that the longitudinally stretched FBG changes its resonant wavelength over time, i.e. a time-wavelength shift of the reflected light is generated [2]. A simple method of demodulating FBG spectral peaks is to use a scanning laser, a tunable optical filter and a photodetector (all parts of an optical spectrum analyzer (OSA) [3] or interrogator [6]). The demodulated power is measured in discrete wavelength steps by OSA. The interpolation of the measured data determines a smooth profile and identification of the resonant wavelength of the reflected signal.

Over the last decade, researchers have addressed various noise effects and asymmetric characteristics of FBG spectral peaks that affect measurement accuracy. In addition to linear methods, the applicability of the wavelet threshold denoising has been demonstrated [7]. Demodulation of multiple weak and noisy FBG spectral peaks has been presented using direct peak-detection algorithms, fitting algorithms, matched filtering, or estimation of cross-correlation resonance point and Mexican-hat wavelet spectral function [8]. Demodulation of distorted FBGs spectra has been focused on their asymmetric side lobes, deformed side lobes, or low extinction ratio of the FBG reflection peaks [9]. Next, 36-point spectra has been used for multi-peak correlation demodulation (4 FBGs) [10]. The characteristics of the sampled FBG spectral peaks have been analyzed and recognized using vector machine support [11] or by machine learning when FBGs overlap or are reconfigured [12]. Wavelet decomposition, Hilbert transformation and fitting methods have already been used [13] for multi-peak detection. Spectral demodulation has been presented using a trained convolutional neural network [14].

Statistical signal detection and the sequential probability ratio test have been two leading theories for binary decision-making in dynamic real-time applications such as the radar detection technology [15], where they play the key role when detecting signals in strongly fluctuating background noise [16], [17]. The sequential probability ratio test technique has been also recently established in other areas such as sensing-based applications [18], [19], communications [20] or biological systems [21]. However, despite the above, there is still lack of real-time de-noising algorithms that dynamically could implement multiple noise fluctuations to and lead to reliable noise

reduction at different Signal-to-Noise Ratio (SNR) scenarios in optical sensing technologies.

Recently, the IEEE Communications Society established the Integrated Sensing and Communication (ISAC) emerging technology initiative [22]. It looks for enabling technologies that combine sensing and communication systems to utilize resources efficiently and even to pursue mutual benefits. In the optical telecommunication parallel, transmission demand-based spectrum prediction algorithms target to improve available bandwidth utilization and throughput of optical lines, reduce delay, and achieve fair transmission to users [23], [24]. We have recently proposed the concept of sharing a common optical fiber for FBG sensing and telecommunication services, benefiting from the occupancy of sensing FBGs [25].

Onward, in this paper we propose a novel efficient algorithm for denoising and statistical detection of FBG spectral peaks in sensing applications implemented in a standard single-mode fiber (SMF). Computing of the denoising dynamic statistical threshold (DDST) is based on implementing non-linear bandwidth attenuation within the SMF, background noise fluctuations, influences of short-term interferences, spectral distortions near FBG spectral peaks and SNR adjusting via probability of false alarms (p_{FA}). The novelty DDST detection algorithm also improves detection robustness where adjacent FBG spectral peaks are overlapped, as the DDST partially follows the shapes of the FBG spectral peaks. The proposed algorithm is applicable for any spectral power dynamics or SNR. It allows to reduce the conventionally pre-reserved operational bandwidths of FBG sensors (via dynamic windowing), brings significant noise reduction and improves SNR and detection reliability. Our experimental results (obtained by two OSAs within the SMF optical sensor network [15], [26]) show reliable adjacent FBG spectral peaks differentiation and a recognition independent of their "pattern" shapes.

The rest of the paper is organized as follows. Section II. formulates problems with the effects of instrument noise, SMF attenuation, overlap of adjacent FBG spectral peaks and noise interferences. Section III. presents the proposed SNR-based DDST detection algorithm using the sliding wavelength window technique and the principle of statistical detection, including mathematical basis. Section IV. comprises simulation results, discussion and validation of the proposed DDST statistical detection algorithm, including a comparison with other techniques. Section V. is a conclusion.

II. Problem Formulation

FBG spectral peak sensing tries to "win" every decibel above background noise. Knowledge of the FBG spectral peak shapes is key for many peak-detection algorithms such as: direct, centroid, fitting and interpolation algorithms [6], [10], [11], [12], [13], [27]. All these approaches consider the rise in the background noise because it is very crucial. This occurs due to nonlinear temperature drifts, SMF attenuation, noise interference, overlap and distortion of FBG spectral peaks, FBG demodulation imperfection, and suboptimal signal processing. Also, the background noise evaluation is usually ambiguous due to the noise uncertainty [18].

A. FBG Signal Shape Distortion Caused by Instrumental Influences

It follows from the nature of optical signals that the optical power signal incident on perpendicular plane is a Gaussian distributed random variable. Assume that the narrowband optical power signal spectrum reflected from an ideal FBG is a Gaussian distributed random variable [28], [29] too with a statistical mean power at the Bragg resonant wavelength $\mu_B \equiv \lambda_B$, and spread described by a standard deviation, σ_B. A Probability Density Function (PDF), which describes the distribution of the reflected power from a FBG as a function of wavelengths λ within the signal bandwidth, is given as

$$f(\lambda_B) = \frac{1}{\sigma_B \sqrt{2\pi}} \exp\left[-\frac{(\lambda - \lambda_B)^2}{2\sigma_B^2} \right]. \qquad (1)$$

Assume optical signal reflected by FBG spectral peak is demodulated by an ideal unipolar demodulation photodiode in a power-wavelength domain. Our next consideration is given to both discrete sweeping and processing along the bandwidth. The integration nature of the discretely measured power transforms the smooth Gaussian distribution to a stepwise type of a binomial distribution [28], [29]. In fact, the discrete FBG spectral peak represents the signal energy E_S measured in a specific discrete sequence of a number of L wavelengths Λ_l. The $l \in (1, 2, ..., L)$ indicates wavelength sample indices. The binomial pdf with discrete probabilities p (of FBG signal occurrence at a given quantization level for l^{th} wavelength) is

$$Bi(L, p) = \frac{L!}{l!(L-l)!} p^l (1-p)^{L-l}. \qquad (2)$$

The generated stepwise instrumental error can be obtained by subtracting (1) and (2)

$$\varepsilon_B(\lambda; L, p) = f(\lambda_B) - Bi(L, p). \qquad (3)$$

However, other imperfections in the production of FBGs or suboptimal signal processing by analogue or discrete equipment may cause an additional increase of noise or FBG spectral shape distortions [1], [2], [3], [7], [9], [10], [11], [12], [27]. In [6], [12], [14], a different wavelength resolution (78 or 156 pm) was obtained by the so called white-light interrogation or 5-10 pm by the oversampling interrogation, respectively. Instrument errors ε_{instr} can be either constant, linear (e.g. offset additions) or nonlinear (e.g. photodiode thermal voltage bias). Some may occur under specific operational conditions and/or in a certain wavelength span.

B. Effects of SMF Attenuation

The attenuation of SMF is caused by two factors, absorption and scattering. Recommendation ITU-T G.652 [30] describes geometrical, mechanical and transmission parameters of the SMF and cable originally optimized for the use in the 1310 nm and 1550 nm wavelength regions. This Recommendation allows the attenuation factor up to 0.3 dB/km from 1530 to 1565 nm and up to 0.4 dB/km from 1310 to 1625 nm wavelength regions (according to the ITU-T G.652.D). This Recommendation also allows operation in other wavelength regions and provides specified scattering loss.
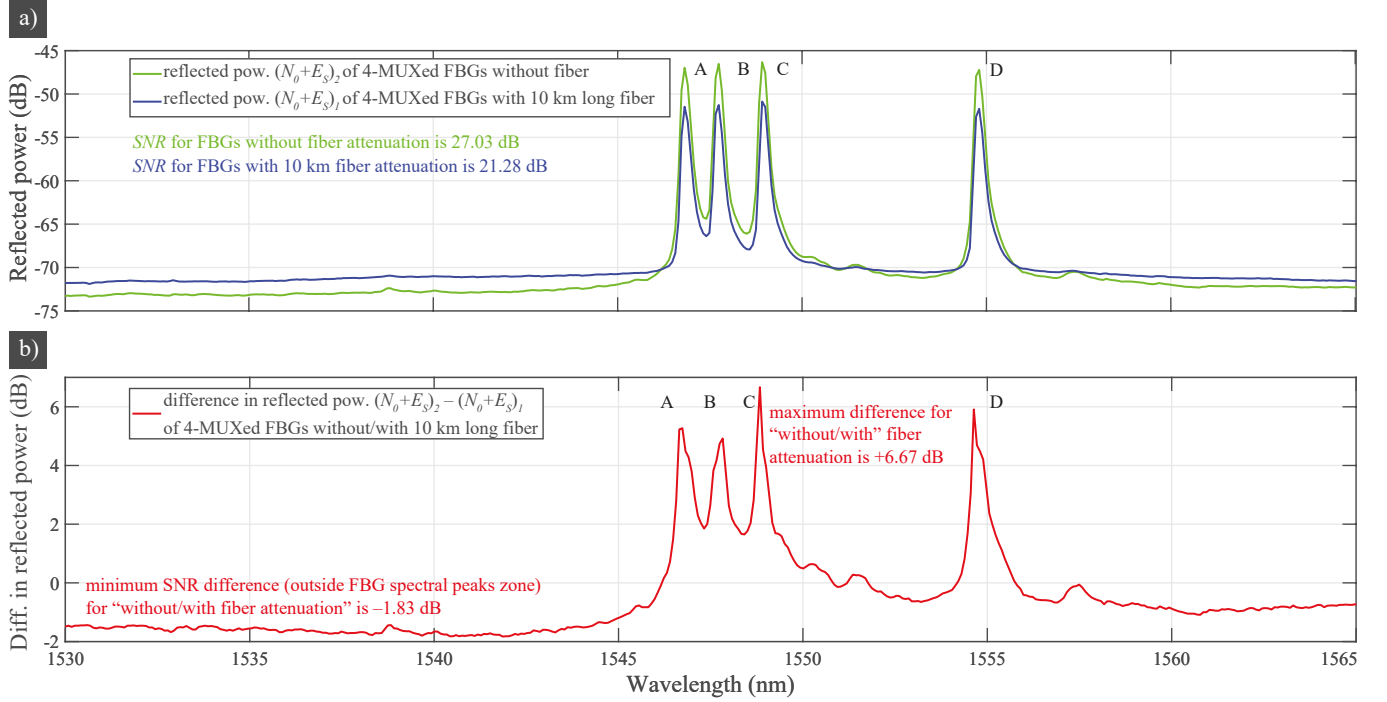
Fig. 1. Demonstration of compound reflected power behavior composed of background noise N0 and 4-MUXed FBGs (A, B, C and D) energy Es: a) $(N_0 + E_s)_1$ when 10 km long SMF was attached (blue) and $(N_0 + E_s)_2$ when no fiber was attached (green), b) showing difference $(N_0 + E_s)_2 - (N_0 + E_s)_1$.

The SMF attenuation is a function of a wavelength, $f_{SMF} \approx f(\lambda)$ and is not linear for different SMF wavebands. The SMF attenuation coefficient can also vary depending on the production quality, ageing, temperature, pressure, stress, bending, and other external factors. Our example shown in Fig. 1 demonstrates the compound $(N_0 + E_s)$ background noise N_0 (caused by interrogator and SMF reflection) and the reflected energy of spectral power peaks E_s from 4 multiplexed (4-MUXed) FBGs A, B, C and D. In Fig. 1a), $(N_0 + E_s)_1$ is shown when a 10 km long SMF (type G.652.D) is attached to the 4-MUXed FBGs (shown in blue) and, $(N_0 + E_s)_2$ when no fiber has been attached (shown in green). The measured SNR with 10 km fiber is 21.28 dB, while without fiber attenuation is 27.03 dB. Fig. 1b) shows $(N_0 + E_s)_2 - (N_0 + E_s)_1$. As it becomes clear from Fig. 1b), adding standard 10 km SMF to the 4-MUXed FBGs causes increase of reflected background noise by approximately 1.83 dB. However, the reflected power of the 4-MUXed FBGs drops up to 6.67 dB.

C. Effects of Overlap with other FBGs

In a number of conventional FBG sensing applications, FBG spectral peaks shift in fixed non-overlapping wavelength windows, where the FBG spectral peak powers exceed experimentally fixed pre-set constant threshold level. We assume Gaussian shape approximation (1) and equal magnitudes for all FBG spectral peaks in the following three paragraphs, just for illustration.

In some multisensory dynamic applications, several FBGs are deployed in a serial connection along the SMF, each having own but different resonant wavelength, [10], [13]. It has to be ensured that any forced wavelength shifts do not overlap with the FBG spectral peaks during sensing system operation. Lateral wavelength shift of FBG spectral peaks is expected and allowed, but the overlap is not allowed. Applying Bragg resonant wavelengths λ_{B_1}, λ_{B_2} and standard deviations σ_{B_1}, σ_{B_2} of two Gaussian FBG power spectral peaks, respectively, we derived the compound pdf of the two overlapping spectral peaks by using [27], [28] as follows

$$pdf(\lambda_{B_1}, \lambda_{B_2}) = \frac{\sqrt{2}}{\sqrt{\pi}(\sigma_{B_1} + \sigma_{B_2})} \exp\left(-\frac{\lambda - \lambda_{B_1}}{2\sigma_{B_1}^2}\right) + \frac{\sqrt{2}}{\sqrt{\pi}(\sigma_{B_1} + \sigma_{B_2})} \exp\left(-\frac{\lambda - \lambda_{B_2}}{2\sigma_{B_2}^2}\right). \tag{4}$$

Fig. 2 illustrates the incoherent adding of spectral power signals of two approaching adjacent Gaussian FBG spectral peaks (normalized in both, the wavelength and power) with a wavelengths overlap rate from 1 % to 90 % on compound power increase. This was obtained using (4). A 60 % overlap is shown in Fig. 2c) where the level of compound power attenuation achieves the full width at half maximum (FWHM). When the wavelengths overlap is 70.7 %, see Fig. 2d), the compound power is represented by two-sided Gaussian spectrum with a flat peak at a power level +21 % above the "non-overlapping normalized power max" level. Finally, if identical FBG spectral peaks will completely overlap and the FBGs attenuation will be doubled, resolving of overlapped FBGs will require some tracking or recognition techniques.

To ensure the proposed method can be easily applied, it is important to reliably estimate the "safe" approaching limit for the FBG spectral peaks. This can be obtained from Fig. 3. A "suitable" general limit can be set below 0.4. For a more robust performance, the limit might be 0.6-0.7.
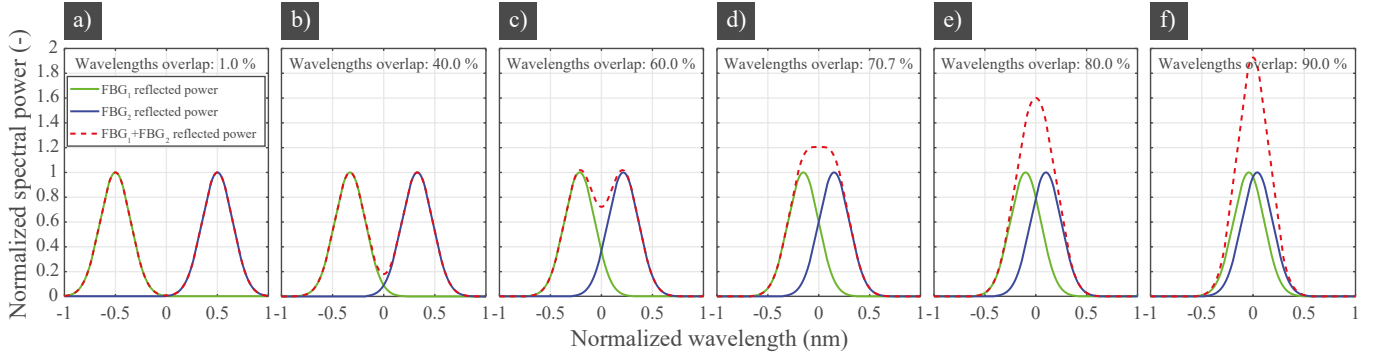
Fig. 2. Approaching of two normalized Gaussian FBG spectral peaks when wavelengths overlap: a) 1%, b) 40%, c) 60%, d) 70.7%, e) 80%, f) 90%.
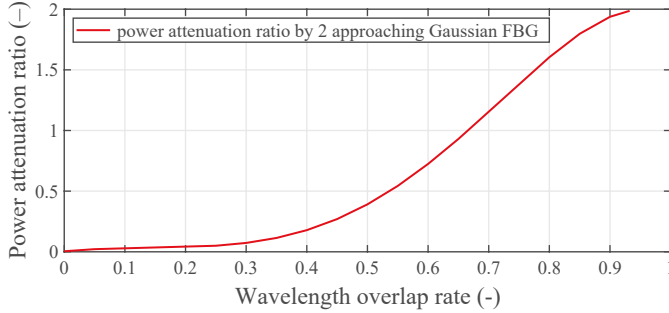

Fig. 3. Attenuation dependence based on overlap rate of two Gaussian-shaped FBG spectral peaks as calculated from Fig. 2 for the midpoint "0" as a function of their approaching.

To illustrate the attenuation dynamics of the approaching FBGs spectral peak, we present another example in Fig. 4a). Here, wavelengths of FBG spectral peaks A and B are fixed during the experiment lasting 13 scanning periods. On other hand, wavelengths of C and D FBGs are shifting during this measurement until $\lambda_C = \lambda_D \approx 1554.6$ nm. At this moment, the attenuation caused by the two overlapped FBGs increases by over +3 dB (see also the asterisked blue line in superimposed plot in Fig. 4b)), to compare it to the non-overlap spectral power values.

D. Effects of Background Noise Interference

FBG multi-peak sensing and telecommunication services aim to increase the system spectral efficiency [10], [13], [14], [20], [22]. However, data must be protected against mutual interference from other services carried by SMF when its spectrum is densely occupied [25]. The FBG sensing system is also easily affected by the harsh environment (wind, rain, vibrations etc.). This makes the demodulated FBG spectrum noisy. The signal denoising is necessary and is done by post-processing after data acquisition. FBG denoising techniques could be Wavelet thresholding, empirical mode decomposition, or compressive sensing algorithms [31]. All these techniques result in certain SNR. From the subsystem's point of view, SNR can then be quantified on both, its input or output with different values as follows

$$SNR_{in} = \frac{E_{in}}{N_{0in}}, \quad SNR_{dBin} = 10\log_{10}\left(\frac{E_{in}}{N_{0in}}\right), \quad (5)$$

$$SNR_{out} = \frac{E_{out}}{N_{0out}}, \quad SNR_{dBout} = 10\log_{10}\left(\frac{E_{out}}{N_{0out}}\right). \quad (6)$$

III. PROPOSED ALGORITHM

A. Applicability of the Proposed Algorithm

To introduce the applicability of the proposed algorithm, we first present a conceptual schematic of the interrogator for scanning SMF with FBG sensors and determine their resonant wavelengths. This is shown in Fig. 5. The presented diagram can be altered as needed by the application. The proposed SNR-based denoising dynamic statistical threshold (DDST) detection algorithm is applied in the FBG signal and data processing subsystem.

The interrogator works as follows. The light source sends appropriate optical scanning signals into the SMF with FBG sensors, via an optical circulator (OC). Each of the FBG sensors reflects a proportional part of the optical signal energy back into the OC to redirect signal into an optical-to-electrical (OE) conversion unit. Here, the tunable narrowband optical filters ensure accurate wavelength measurements and resolution. A unipolar photodiode serves as a photodetector (PD) that provides an OE conversion. The unit contains optical (EDFA) and electrical (OPA) amplifiers to boost the signal as needed.

After the OE conversion, FBG signal is processed by the analog-to-digital converter (ADC). The random access memory (RAM$_1$) continuously stores the received data resulted from the tuning of the optical filter at the input of the FBG signal/data processing unit.

Then the stored data are processed in the detector of FBG spectral peaks. Here, a conventional detector of FBG spectral peaks seeks for a values above a fixed set threshold. However, trend detectors use artificial intelligence (AI) algorithms to analyze the shapes of FBG spectral peaks to produce shape classifications (as classifiers of shapes). Unlike both these detectors/classifiers, our proposed SNR-based DDST detection algorithm benefits from statistical analysis of the background noise. The operation of the DDST algorithm is described in following subsections III.B and III.C. The statistical threshold automatically adapts to arbitrarily complex noise or interference conditions, or to partial overlap of FBG spectral peaks. This will be shown experimentally. The DDST detection algorithm can also be used for a preliminary denoising in previous types of detectors/classifiers.
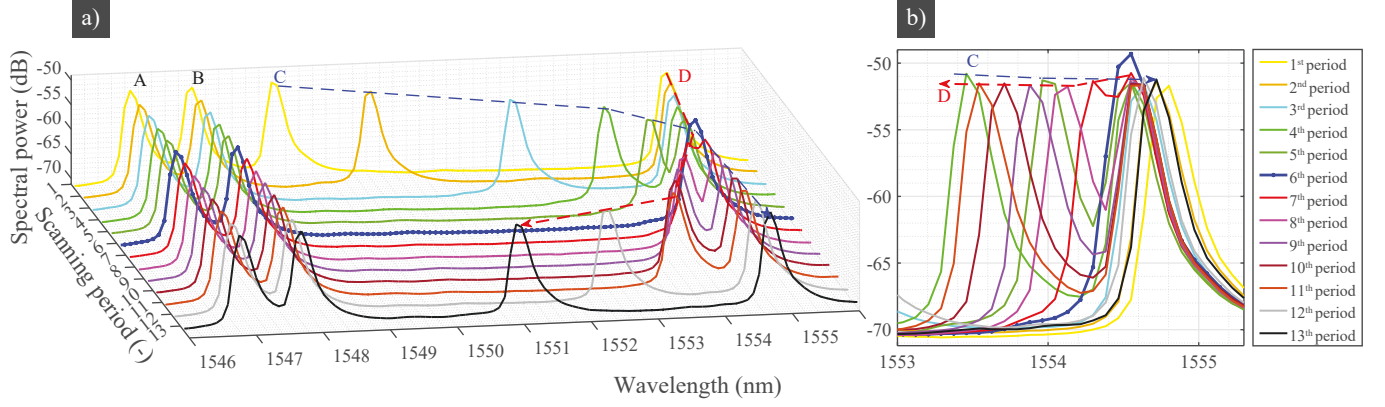
Fig. 4. Demonstration of spectral power incoherent addition under dynamic changes of C and D FBGs obtained during 13 measurement periods, when C FBG shifts 1st to 6th periods and D FBG shifts 7th to 13th periods: a) 3D plot, b) 2D superimposed plot.
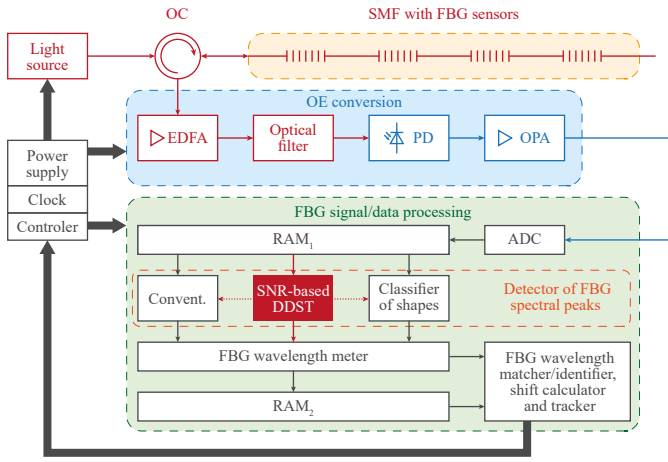

Fig. 5. General schematic diagram of the interrogator with proposed SNR-based DDST detector.

Fig. 6. SNR-based dynamic statistical threshold detector of FBG spectral peaks.

The signal then enters an FBG wavelength meter to determine the measured signal wavelength. It uses direct, centroid, fitting or interpolation algorithms, and matches it to the FBG resonant wavelength. Determined FBG resonant wavelengths are stored in RAM_2. This processing is repeated by each measurement cycle. The target FBG wavelength shift can be obtained via inter-period matching. This provides the user with information about the dynamics of external physical factors acting on individual FBGs.

B. Operation of the Proposed Algorithm

The proposed DDST detection algorithm is schematically shown in Fig. 6. It targets denoising and identifying of FBG spectral peaks powers that are above dynamically calculated statistical threshold in order to improve the post-photodetection SNR. This can be done independently of the prior knowledge of the shape of FBG spectral peaks. The DDST algorithm also aims to improve FBG spectral peaks resolving if they become partially overlapped or they are affected by interference from neighboring narrowband signals from services supported by SMF [25]. The proposed algorithm will also account for the background noise fluctuations.
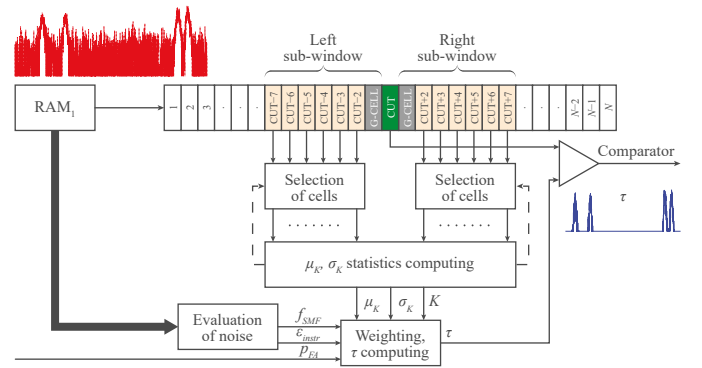
As shown in Fig. 6, digitized sums (background noise plus FBGs' reflected powers, in spectral domain) are continuously stored in an N-cell shift register. These acquired spectral power values are stored along with n discrete wavelength steps, $n \in (1, 2, ..., N)$. The pre-defined sliding wavelength window of length L systematically slides and operates across the N-cell register. This sliding window consists of the cell under the test (CUT), $2G$ neighboring guarding cells (G-CELL) and K adjacent cells located left and right of CUT. K is defined by a number of discrete wavelength steps along the FBG bandwidth. The left sub-window, see Fig. 6, contains cells from $CUT - G$ to $CUT - k$ and symmetrically the right sub-window contains cells from $CUT + G$ to $CUT + k$. A number of cells $K = 2k = L - 2G - CUT$ is used to compute the so called "local statistics" around CUT, the mean μ_K and the standard deviation σ_K.

The DDST detection algorithm statistically evaluates the background noise along N wavelength steps. As a result, the approximation function of the SMF attenuation, f_{SMF}, and the instrument error, ε_{instr}, are obtained and used to adjust the threshold, τ. The f_{SMF} and ε_{instr} are periodically updated. The targeted probability of false alarms p_{FA} is a constant slowly varying in time (see the experimental part).

The comparator based on described inputs then decides which cells powers are above the statistical threshold value.

C. Mathematical Basis of the Proposed Algorithm

The computation of threshold level τ is based on continuous evaluation of the statistical parameters μ_K and σ_K along the sliding wavelength window, which consists of K cells around the CUT. Sometimes, the K number can differ from the L number of wavelengths belonging to a typically measured FBG bandwidth. Prior to calculating μ_K and σ_K from the background noise, various techniques of selecting "suitable cells" can be used to protect the threshold from the inclusion of the sudden interference or power intrusion/leakage from the adjacent cells (caused by discretization of FBG spectral peaks, especially in a dynamic power environment). These techniques can modify the needs for surrounding guarding cells. Selection techniques can be dynamically chosen and controlled by a feedback, so that the system is automatically able to adapt cells selection even under difficult detection conditions. In addition to μ_K, σ_K and K, we recommend implementing three additional input parameters to adjust the statistical threshold to the desirable level:

a) the level of probability for a false alarm (p_{FA}),
b) the instrument error ε_{instr},
c) the offset function f_{SMF} describing fiber attenuation along the used wavelength span.

Detection of an unknown but assumed Gaussian shape spectral power signal at a presence of the background noise requires sufficient dynamic bandwidth of the photodetector. Choosing a sufficient sliding wavelength window width K around CUT is recommended for reliable computing of μ_K and σ_K. Using selection techniques and multiple levels of detection threshold for dynamic background noise behavior is preferable. Applying the Bayesian decision theory [31], [32] with decision criteria [33] for the background noise and FBGs spectral power PDFs, the optimized general threshold decision criterion $T(E)$ with the threshold τ is given as follows

$$T(E) := \frac{N_0}{N_0 + E_S} e^{-\frac{E_{CUT}}{N_0(N_0+E_S)}} \gtreqless \tau \Rightarrow \begin{cases} \text{YES} \,|\, \text{LOG1} \\ \text{NO} \,|\, \text{LOG0} \end{cases} \quad (7)$$

where the N_0 is the mean of a Gaussian random amplitude noise, E_s is anticipated FBG signal energy and E_{CUT} is the energy obtained in a CUT. Due to the nature of the unipolar photodetector, its electrical signal at the output is Rayleigh distributed random variable with the variance is as follows

$$\sigma_{N_0+E_S}^2 = \sigma_{N_0}^2 + \sigma_{E_S}^2 = \sigma_{N_0}^2 \left(1 + \frac{\sigma_{E_S}^2}{\sigma_{N_0}^2}\right) \equiv$$
$$\equiv \sigma_{N_0}^2 \left(1 + \frac{E_S}{N_0}\right) \equiv \sigma_{N_0}^2 \left(1 + SNR\right). \quad (8)$$

However, other effects may distort the shape of the PDF of the background noise as well as the shape of PDF of the FBGs, as shown in Fig. 7. In general, the threshold value τ always intersects both of these PDFs. The resulting probability areas are as follows: I – probability of correct FBGs detection (integral from τ to maximum demodulated power under the red curve), II – probability of false alarms i.e. false FBGs detection (integral from τ to maximum demodulated power under the blue curve), III – FBGs detection loss (integral from
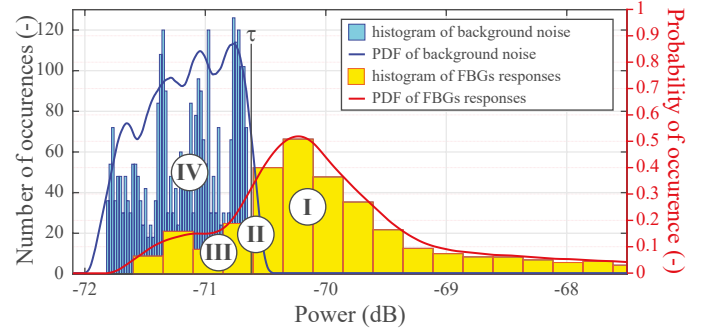

Fig. 7. Principle of statistical threshold detection based on desired p_{FA} setting.

minimum demodulated power to τ under the red curve), IV – probability of correct noise detection (integral from minimum demodulated power to τ under the blue curve). The areas II and III should be carefully considered when computing the threshold. Much more attention should be paid to the area II, because its high p_{FA} may cause false positive increase of FBG wavelengths numbers. These are the cases when a such FBG does not exist (NO-FBG) and the background noise could exceed the detection threshold thus causing these false detections. This would lead to fatal measurement errors. The p_{FA} can be found using [28], [32] as follows

$$p_{FA} = \int_{\tau}^{\infty} p\left(N_0 + E_S \,|\, \text{NO–FBG}\right) dE =$$
$$= \int_{\tau}^{\infty} \frac{E_{CUT}^2}{\sigma_{N_0+E_S}^2} \exp\left(-\frac{E_{CUT}^2}{2\sigma_{N_0+E_S}^2}\right) dE. \quad (9)$$

This truncated pdf is limited by the threshold τ and following [33], τ has been derived as follows

$$\tau = N_0 E_S \ln \frac{1}{p_{FA}}. \quad (10)$$

Similarly, the probability of correct FBG spectral peaks detection P_D (shown in Fig. 6 as the area I where FBG exists and decision about FBG existence is correct) using [28], [32] can be derived

$$p_D = \int_{\tau}^{\infty} p\left(N_0 + E_S \,|\, \text{FBG}\right) dE =$$
$$= \int_{\tau}^{\infty} \frac{2E_{CUT}}{N_0 E_S} \exp\left(-\frac{E_{CUT}^2}{N_0 E_S}\right) dE. \quad (11)$$

It is possible to independently measure both, the noise and FBGs probability density functions, as can be seen from the histograms in Fig. 7. But, they are not a priori exactly known. They change under fluctuations of background noise or interferences. Therefore, the threshold τ must not be constant. It must dynamically incorporate all possible fluctuations. The DDST detection algorithm incorporates the instrumental error ε_{instr}, approximation function of SMF attenuation f_{SMF}, measured additive noise and signal power $(N_0 + E_s)$ parametrized by μ_K and σ_K along the sliding wavelength window. The anticipated minimum-to-maximum FBGs signal power ranges

from E_{min} to E_{max}. It is parametrized by p_{FA} (based on SNR) and by sliding wavelength window ratio as follows

$$\tau = \varepsilon_{instr} + f_{SMOF} + (N_0 + E_S)\mu_K\sigma_K + \\ -\frac{E_{max} - E_{min}}{\ln\frac{1}{p_{FA}}}\frac{K - G}{K}. \quad (12)$$

Based on the obtained statistical threshold τ, the comparator at its output will generate the signal pulse presuming the existence of the FBG spectral peak in the given CUT at the n_{th} wavelength.

IV. RESULTS OF SIMULATION, DISCUSSION AND VALIDATION

As mentioned in the previous section, we assume that background noise is generated mainly by the OSA photodetector, optical fiber and interconnections. An example of the measured reflected background noise along the waveband is shown in Fig. 8.

Fig. 8a) shows in blue the attenuation of a 5 km long SMF approximated by the 2nd order polynomial function f_{SMF}. The green line in Fig. 8b) is the reflected noise floor caused by the first OSA with a C-band mean level $\mu = 73.56$ dB and standard deviation $\sigma = 0.15$ dB. The connected pigtail increases the mean reflected power by negligible 0.02 dB, see the brown line. The black trend line f_{SMF} indicates a linear offset along the used wavelength span caused mainly by an active system element, the photodiode. However, the 10 km long SMF significantly contributes to the reflected background noise increase from 1.5 to 1.8 dB having its maximum at a wavelength of 1552 nm (shown in orange in Fig. 8b)). After adding another 5 km of SMF, the total reflected background noise shown in red increases even more, by 0.75 to 0.95 dB, see also the 2nd - order polynomial summary approximation f_{SMF} in magenta.
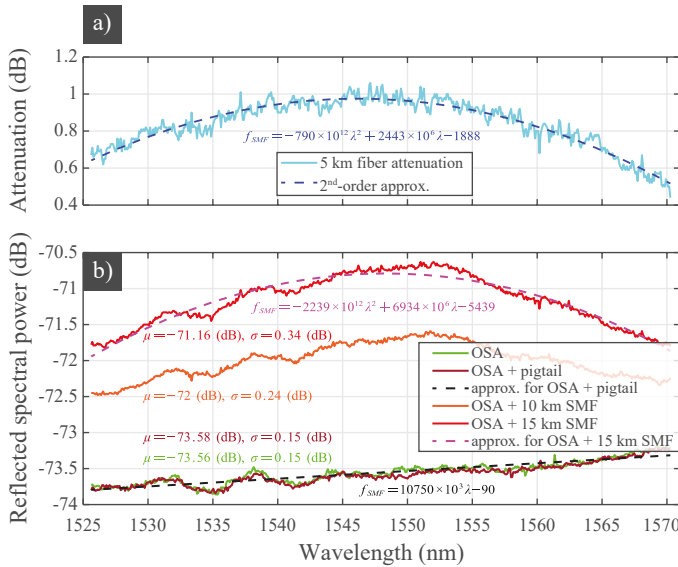

Fig. 8. Measured reflected spectral power as a background noise and its approximation along C-band and beyond: a) full duplex attenuation of 5 km SMF, b) pigtail, 5 km and 10 km SMF attenuation influence on reflected signal power.
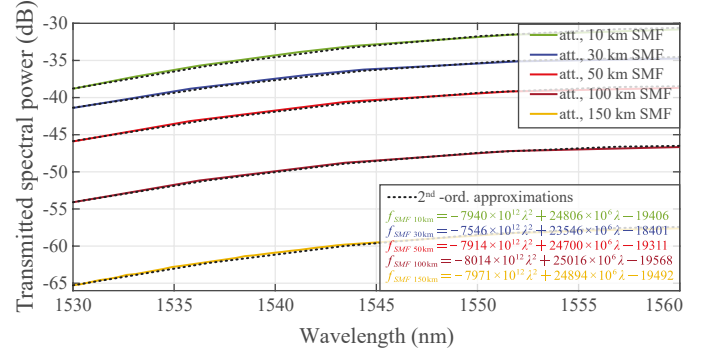

Fig. 9. Background noise measured as a transmitted power of wideband light source attenuated by 10, 30, 50, 100 and 150 km SMFs, respectively.

Another example of transmitted power attenuation is based on 250 nm wideband light source operating from 1550 to 1800 nm by another OSA. In Fig. 9, the transmitted spectral power is shown when using 10 to 150 km optical fibers. The attenuation spectral wavelength dependency change was measured to be up to 8 dB along the C-band. To fit these curvatures, it was necessary to find the mathematical model. The obtained results are shown again in Fig. 9. Good fit between experimental and mathematical results can be seen. To obtain the above results, the intrinsic 20 pm resolution of the OSA was improved by applying the post-demodulation wavelength upsampling [6] that resulted in approximately 3.43 pm resolution.

A. FBG Spectral Peaks Windowing

Dense spectral spacing and any unexpected events affecting FBGs cause a spectral overlap. Fig. 10 shows a simple FBGs detection and the windowing when 4-MUXed FBGs (A, B, C and D with occupied bandwidths of about 450 pm at FWHM) at high $SNR_{in} > 20$ dB were used. The 2nd-order approximation of the background noise (f_{SMF} and ε_{instr}) is included. First, the three conventional thresholds +1.2 dB (green dot-and-dash line), +2 dB (brown dot-and-dash line) and +3 dB (blue dot- and-dash line) above the 2nd-order background noise approximation f_{SMF} are used. Besides the correct detection of the A, B, C and D FBG spectral peaks, the lowest threshold inappropriately generates false alarms from low-level interferences, such as the in the short wavelength section around 1552 nm (indicated by the green line). Therefore, it is not appropriate to use the windowing for a low level threshold addendum of +1.2 dB. The higher the threshold, the narrower is the window, see brown and blue lines. To summarize Fig. 10, for a reliable and simple DDST-based windowing, the background noise approximation f_{SMF} is recommended to be used. A simplified windowing approach can be used when occupancy of FBG spectral peaks are required in a noiseless environment with the high SNR. Such a system with a periodically updated threshold for efficient spectrum utilization for sharing a common optical fiber for both sensing and telecommunication services in more complex environment was demonstrated in [25]. The requirements for automatic
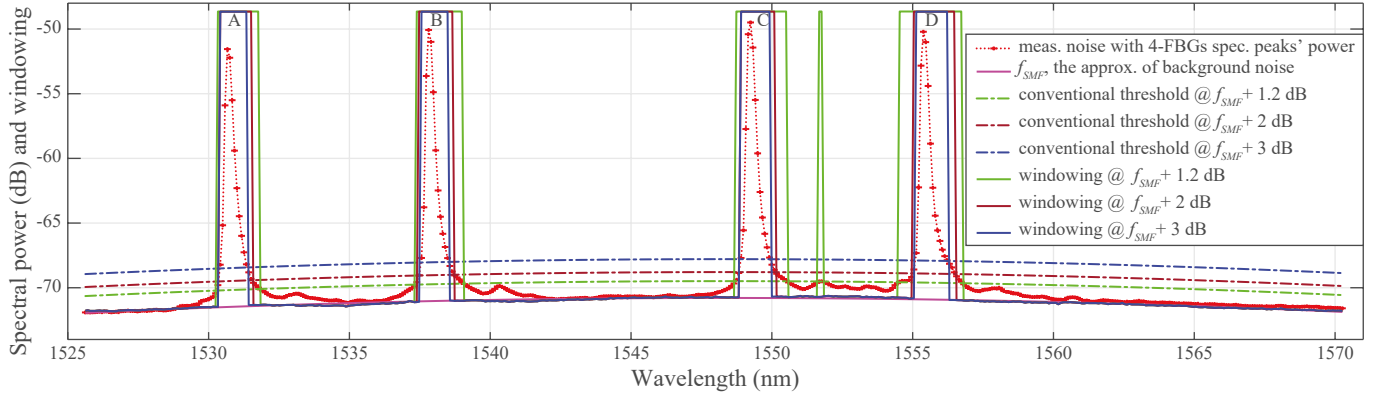
Fig. 10. Windowing for 4-MUXed FBGs at three conventional detection thresholds of +1.2 dB (green), +2 dB (brown) and +3 dB (blue) above 2nd-order approximation of background noise (noise floor and fiber attenuation included).
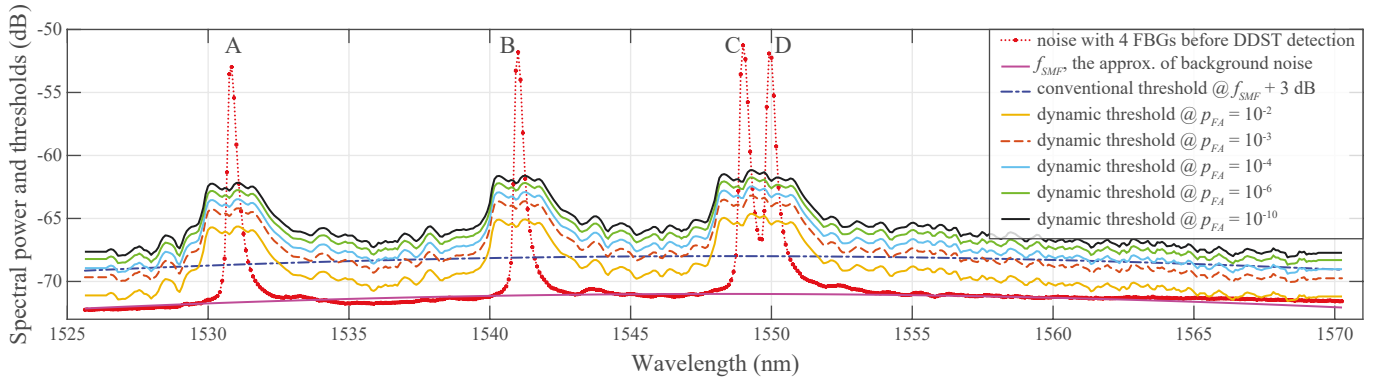

Fig. 11. Dynamic statistical threshold detection of 4-MUXed FBGs (A, B, C and D), based on SNR implementation via p_{FA} at high SNR.

threshold adjustment and occupancy robustness around FBGs are also discussed there.

B. FBG Spectral Peaks Detection Using the Dynamic Statistical Threshold Under High Input SNR

This subsection describes an example of a real adaptive detection of 4-MUXed FBGs spectral peaks (2 solitary and 2 adjacent) using the full DDST detection algorithm. Based on (12), the adaptive dynamic thresholding results are shown in Fig. 11 for high $SNR_{in} > 20$ dB. The implementation of the fSMF and ε_{instr} makes it possible to obtain approximate levels of detection thresholds with the presence of background noise. A periodic verification of background noise offset found in FBGs-free spectral locations is possible and has been used in our Fig. 11 example. Because the presence of FBG spectral peaks causes an increase in μ_K and σ_K, the threshold level increases significantly.

The acceptable probability of false alarms ranges from a very high $p_{FA} = 10^{-2}$ to an extremely low $p_{FA} = 10^{-10}$. The threshold τ is parameterized by an anticipated energy range of the FBGs signals from $E_{s_{min}}$ (being close to the background noise approximation) up to $E_{s_{max}} \approx +20$ dB above the background noise. The τ is adjusted by the width of the sliding wavelength window to account for increases in σ_K when it is too narrow. The more severe the p_{FA} requirement is, the higher τ will be computed. If a lower threshold level is

applied, a higher number of detected discrete spectral "points" from an FBG spectral peak will be obtained, see asterisks in Fig. 11. It leads to a nearly full number of wavelengths within the section occupied by the FBG and thus to a safer FBG spectral windowing [25]. Such pre-processing could lead to a better detectability of FBG spectral peak shapes and their recognition by classifiers.

On other hand, if using higher thresholds is possible, better wavelength measurements and resolving of colliding FBG spectral peaks can be achieved. Then, the proposed DDST detection algorithm also improves resolving the possibility of FBGs resonant wavelengths collision. This is shown in the Fig. 11 example where C and D adjacent spectral peaks (1549 and 1550 nm) have 40 % overlap and are very well resolved by a DDST detector. In contrast, the conventional threshold at $f_{SMF} + 3$ dB completely loses the resolving of C and D FBGs (see the blue dot-and-dash line).

C. Multi-FBG Spectral Peaks Detection Using Dynamic Statistical Thresholding with Two Different Types of FBGs and Different Input SNRs

This section describes an example of an adaptive dynamic thresholding that leads to results shown in Fig. 12 when 4-MUXed FBGs at $SNR_{in} > 20$ dB are interfered by additional FBGs I to X. Each of these additional FBGs with an $SNR_{in} > 15$ dB occupies a narrowband bandwidth of 84 pm
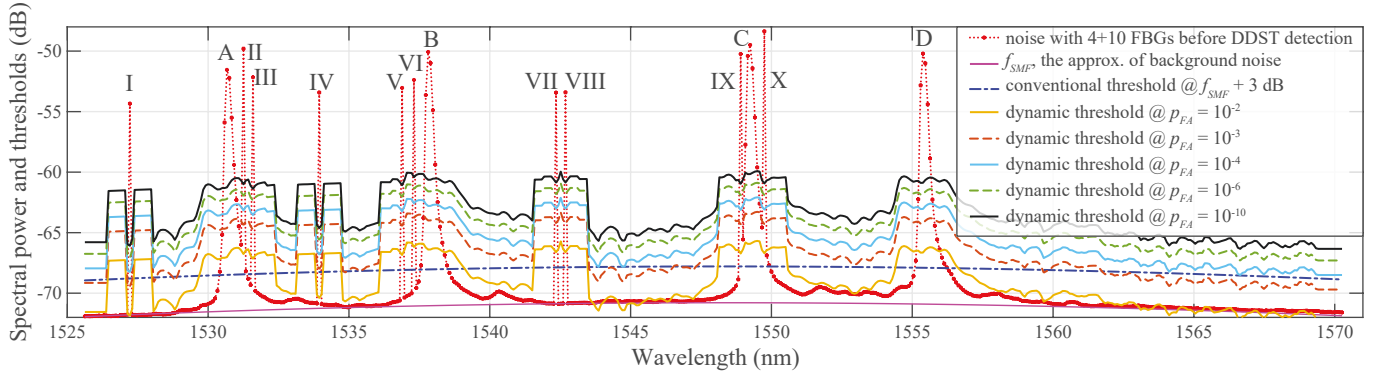
Fig. 12. Multi-FBG dynamic statistical threshold detection based on SNR implementation via p_{FA} at high SNR: A, B, C and D FBGs interfered by I-to-X narrowband FBGs.
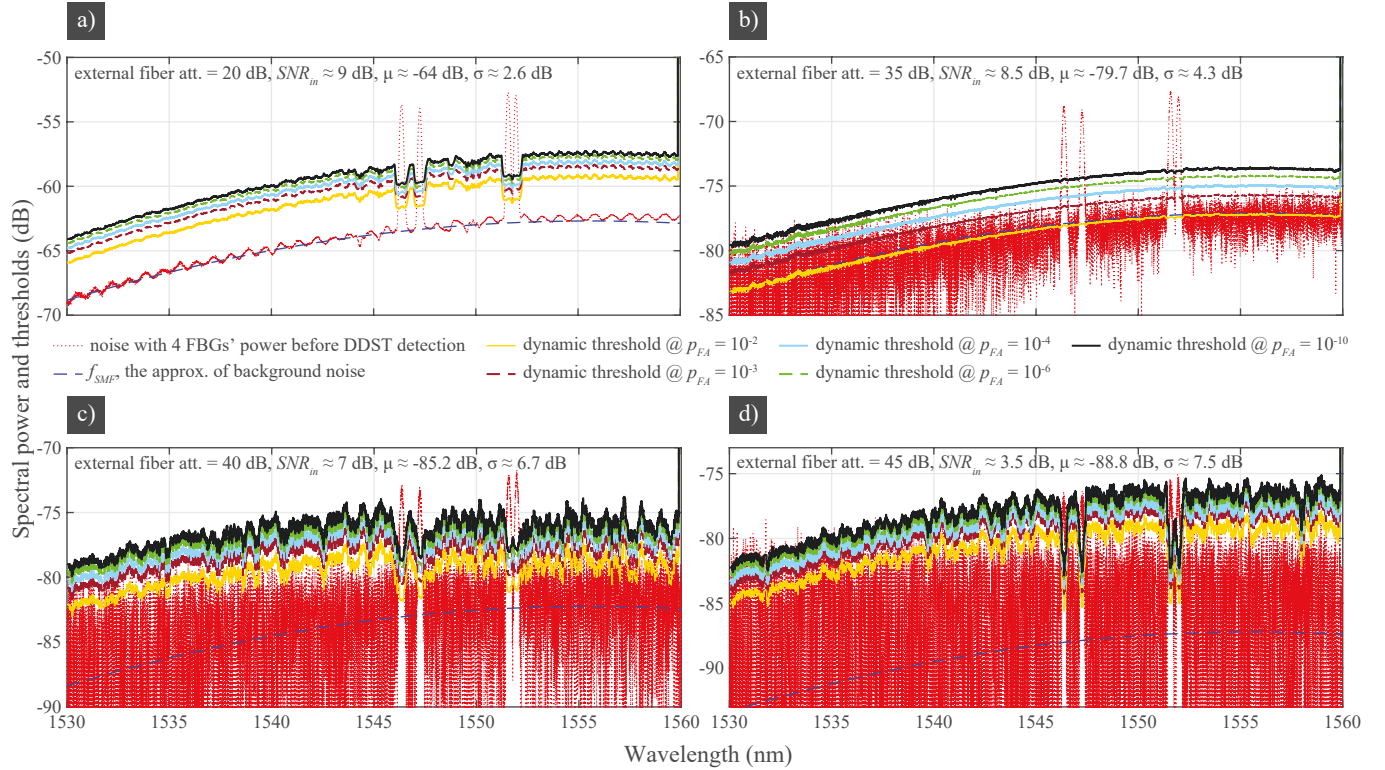

Fig. 13. DDST detection of 4-MUXed FBGs at deep external power attenuation by optical fiber, at low SNR and with moderate to severe noise fluctuations near the detectability level: a) with 20 dB attenuation and $SNR \approx 8.5$ dB, b) with 35 dB attenuation and $SNR \approx 8.5$ dB, c) with 35 dB attenuation and $SNR \approx 7$ dB, d) with 45 dB attenuation and $SNR \approx 3.5$ dB.

at FWHM. Both, the conventional and DDST detections were investigated. They both successfully detected different types of solitary FBGs (I, IV and D) and also the adjacent but not overlapping narrowband FBGs (VII and VIII). However, FBGs V, VI and B were more reliably resolved by DDST detector. When the conventional detector was used to resolve the overlapping FBGs (A, II, III, C, IX and X), the detection collapsed. However, our proposed DDST detection reliably handled the situation, even if only starting from $p_{FA} = 10^{-2}$.

D. FBG Spectral Peaks Detection Using the Dynamic Statistical Threshold Under Low Input SNR

This section describes the applicability of the proposed DDST detection algorithm for 4-MUXed FBGs (2 solitary and 2 adjacent). The FBGs were illuminated with a 250 nm broadband light source from 1550 to 1800 nm. The transmitted signals were observed by OSA with a high-resolution of 3.43 pm. Fig. 13a) to Fig. 13d) illustrates the measured increase in the external fiber attenuation att_{SMF} that was 20, 35, 40 and 45 dB, the standard deviation σ, the fluctuating background noise (especially in the region below 1550 nm), and the degradation of the SNR_{in} at the input of the DDST detector. Fig. 14 is the zoom-in of the situation depicted by Fig. 13. Both figures also show statistical thresholds for $p_{FA} = 10^{-2}$ to $p_{FA} = 10^{-10}$. Fig. 15 shows the zoom-in of the comparative decision making at the output of the DDST detection algorithm (CUT signal minus the threshold).

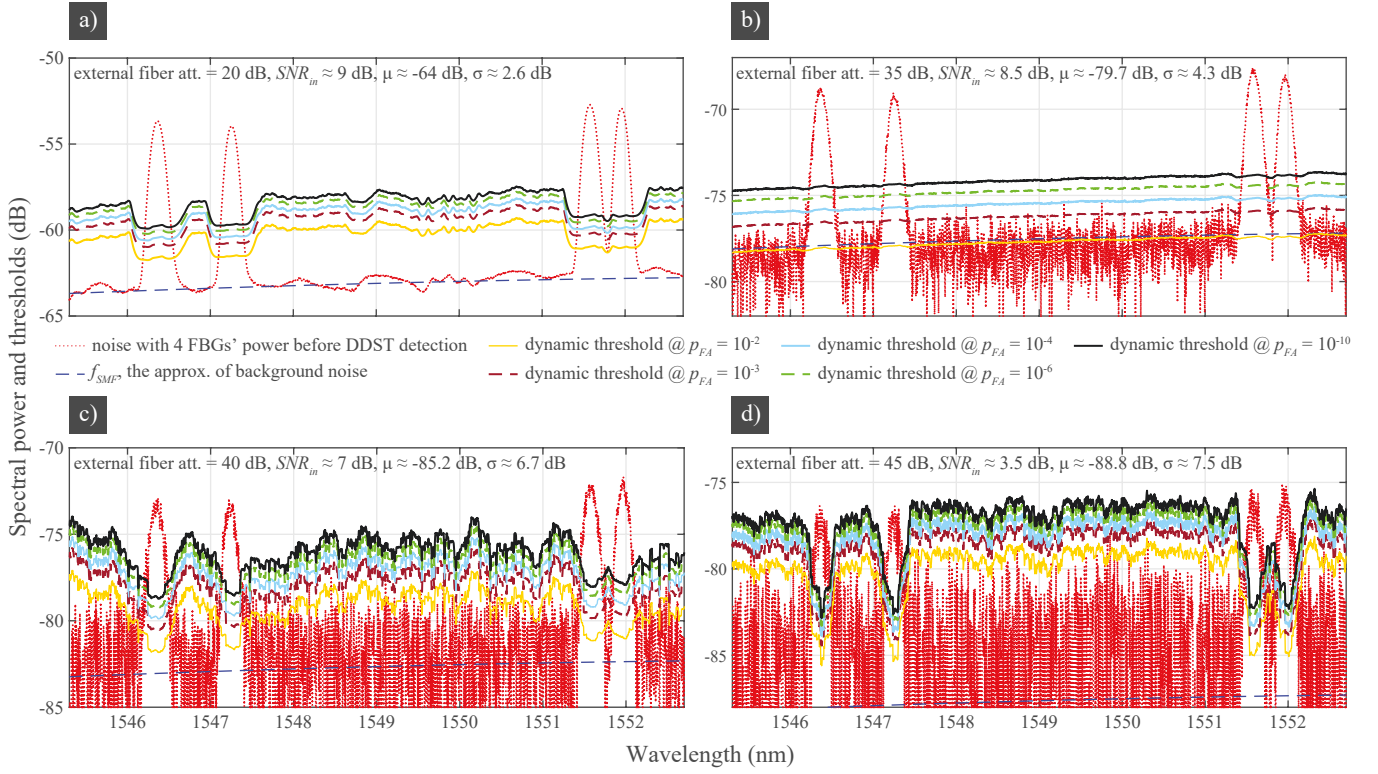Fig. 13a) and Fig. 14a) show a reliable thresholding when

Fig. 14. Detailed DDST detection of 4-MUXed FBGs at deep external power attenuation by optical fiber, at low SNR and with moderate to severe noise fluctuations near the detectability level: a) with 20 dB attenuation and $SNR \approx 8.5$ dB, b) with 35 dB attenuation and $SNR \approx 8.5$ dB, c) with 35 dB attenuation and $SNR \approx 7$ dB, d) with 45 dB attenuation and $SNR \approx 3.5$ dB.

$att_{SMF} = 20$ dB, the inhomogeneous noise environment varied with $\sigma = 2.6$ dB and the measured medium was $SNR_{in} \approx 9$ dB. The output power of FBG spectral peaks dropped to ~ 7 dB despite the threshold was set at $p_{FA} = 10^{-3}$, see Fig. 15a). This drop is a penalty for denoising, getting reliable detection and reliable separation of two adjacent FBG spectral peaks having an overlap of about 40 % under inhomogeneous noise environment.

Fig. 13b) and Fig. 14b) show also smooth reliable denoising and thresholding in degraded conditions of $att_{SMF} = 35$ dB, $\sigma = 4.3$ dB, and $SNR_{in} \approx 8.5$ dB. The above mentioned broadband light source causes increased noise fluctuations leading to occasional pulse noise penetrations above selected thresholds, noticeably around 1535 nm. Since the σ varies along the studied waveband, the output FBG spectral peaks are noisy and some noise residuals occur above the threshold τ at $p_{FA} = 10^{-3}$, see Fig. 15b). Of course, a stricter threshold (like at $p_{FA} = 10^{-4}$) is able to completely remove these noise residuals, see Fig. 14b).

Fig. 13c) and Fig. 14c) show dynamically adapted reliable denoising and thresholding in severely degraded conditions: $att_{SMF} = 40$ dB, increased $\sigma = 6.7$ dB, and $SNR_{in} \approx 7$ dB. The output FBG spectral peaks are noisy. This causes increased σ. Since σ is quite homogeneous alongside of the scanned waveband, only a few noise residuals occur above the threshold at $p_{FA} = 10^{-3}$, see Fig. 15c). As can be seen in Fig. 14c), a stricter threshold (like at $p_{FA} = 10^{-4}$) is able to completely remove observed noise residuals. The most important consequence is over 7 dB increase in the output

power of FBG spectral peaks, see Fig. 15c).

Fig. 13d) and Fig. 14d) show dynamically adapted reliable denoising and thresholding in severely degraded environment: $att_{SMF} = 45$ dB, $\sigma = 7.5$ dB and $SNR_{in} \approx 3.5$ dB. As can be seen, these results in output FBG spectral peaks being noisy. Because σ in the studied waveband is nearly constant, the noise residuals are eliminated by DDST detector at $p_{FA} = 10^{-3}$ (see Fig. 15d)). Further elimination of noise residuals could be achieved using a stricter threshold (e.g. at $p_{FA} = 10^{-4}$). The most important consequence would be a doubled output power of the FBG spectral peaks (8 dB above the threshold τ at $p_{FA} = 10^{-3}$).

In conclusion, as shown in Fig. 15a) to Fig. 15d), a reliable denoising, detection and high level of adjacent FBG spectral peaks resolving are achieved by our novel DDST detection algorithm. The statistical thresholds "follow" the background noise levels, "local statistics" μ_K and σ_K as well as FBG spectral peaks shapes. Despite the fact that the p_{FA} was only 10^{-3}, we were able to successfully detect each 4-MUXed FBGs by the dynamic statistical thresholding. This p_{FA} value was intentionally chosen to reflect high number of wavelength samples (8750) in the studied waveband. This resulted in the maximum of $8750 \times p_{FA} = 8.750$ false alarms, as can be seen in Fig. 15a) and Fig. 15d). A number of false alarms was slightly exceeded in Fig. 15b) and Fig. 15c) cases due to significant changes in the background noise variance. Here, the denoising significantly improved SNR_{out} and smoothen FBG spectral peak shapes, see Fig. 15c) and Fig. 15d).
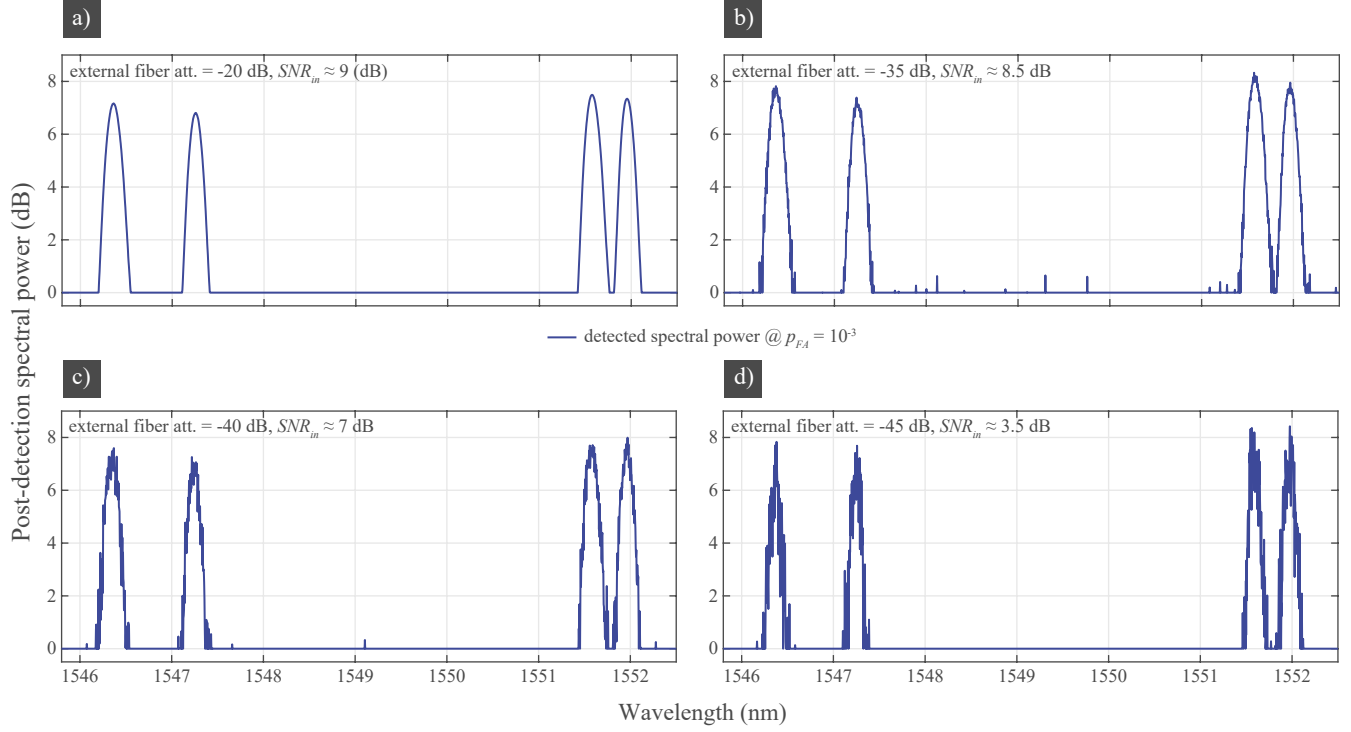
Fig. 15. Spectral power of 4-MUXed FBGs detected by DDST detector above statistical threshold level at $p_{FA} = 10^{-3}$: a) with 20 dB attenuation and $SNR_{in} \approx 9$ dB, b) with 35 dB attenuation and $SNR_{in} \approx 8.5$, c) with 40 dB attenuation and $SNR_{in} \approx 7$ dB, d) with 45 dB attenuation and $SNR_{in} \approx 3.5$ dB.

E. Comparison with Other Techniques

Investigating FBG resonant wavelengths in sensor arrays is a well-established method that is an inherent part of FBG interrogation systems (often with own, sometimes proprietary, algorithms for peak detection and tracking). Typically, most peak detection and tracking methods (direct or fitting) are based on FBG power demodulation with a sufficient FBG reflectivity (up to 90%) thus high SNR (> 15 dB) [4], [6], [34]. Correlation methods trace the coincidence ratio between measured and calibrated reference spectra in order to detect the wavelength shift. They are therefore sensitive to fluctuations of the measured FBG spectral shape. Correlation methods could be used in cases of a lower $SNR \approx 10$ dB and less fluctuating background noise [6]. Transform-based methods and optimization techniques (such as using neural networks or genetic algorithms) require more complex processing. The use of the Wavelet filtering causes the reduction of the number of wavelength samples and requires accurate estimation of both approximate and detailed coefficients for each of transformation stages [6], [35]. Another approach described in [13] applies Wavelet denoising, Hilbert transformation and parabola fitting methods, under $SNR > 11.25$ dB and fluctuations below $\sigma < 1.229$ conditions. In summary, these peak tracking methods depend on the FBG spectrum shapes. With difficulties, they can work only with a limited SNR.

Compared to just described techniques, the proposed SNR-based DDST detection algorithm can detect FBG spectral peaks in severe environmental conditions. We have demonstrated successful operation of our novel method reliably working under -75 dB at $SNR < 4$ dB and having background
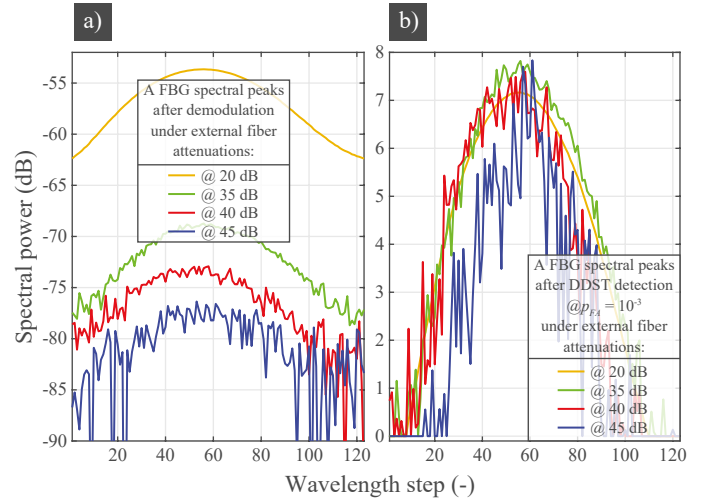

Fig. 16. Comparison of FBG spectral peak shapes under 20, 35, 40 and 45 dB fiber attenuation a) after demodulation, b) after DDST detection by dynamic statistical detector at $p_{FA} = 10^{-3}$.

noise standard deviation of $\sigma > 7$ dB.

In the next step, we will investigate the influence of the proposed algorithm on the standard deviation of noisy FBG signals versus a noiseless reference FBG signal. Then we will compare scenarios from Section IV.D (notably 35, 40 and 45 dB fiber attenuations versus noiseless signals of FBG spectral peaks at 20 dB fiber attenuation).

This is shown in Fig. 16a) where the transmission spectral power of demodulated solitary FBGs along 123 wavelength positions are attenuated by fiber at 20, 35, 40 and 45 dB.
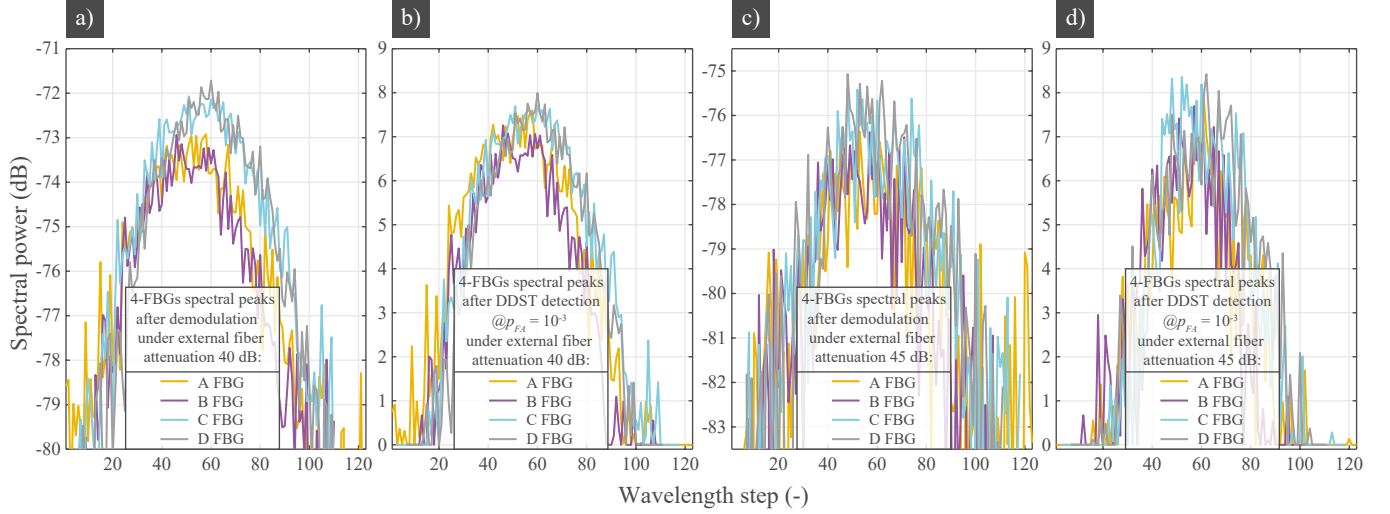
Fig. 17. Comparison of 4 FBG spectral peak shapes: under 40 dB attenuation a) after demodulation and b) after DDST detection at $p_{FA} = 10^{-3}$, under 45 dB attenuation c) after demodulation and d) after DDST detection at $p_{FA} = 10^{-3}$.

In comparison, Fig. 16b) shows the DDST detected shapes of the same FBG spectral peaks influenced by the same fiber attenuation. Here, the detected FBG power is seen as "normalized" in volume and the wavelength range narrowed by $\sim 10\%$.

Fig. 17a) shows the demodulated shapes of spectral peaks of 4-MUXed FBGs along 123 wavelength positions influenced by 40 dB fiber attenuation. In comparison, Fig. 17b) shows the detected shapes under the same conditions. Here is clearly seen, DDST detection results in less shape variance. Similarly, Fig. 17c) and Fig. 17d) compares the demodulated and DDST detected 4-MUXed FBG signals under a 45 dB fiber attenuation. Here it is clearly seen that DDST detected signals are less varying in shape. Again, the DDST detection causes the FBG wavelength range narrowing approximately by $\sim 10\%$.

Finally, Fig. 18 shows the normalized absolute deviation of noisy FBG signals versus the noiseless FBG signal (dB) for the typical solitary FBG spectral peak(s) along the 123 wavelength positions under the fiber attenuation of 35, 40 and 45 dB, and compares it with 20 dB fiber attenuation. In Fig. 18a), the absolute deviation of demodulated signals substantially varies for nearly a half of wavelength positions (1st to 25th and 93rd to 123rd positions). In Fig. 18b), the post-detection absolute deviations for all wavelength positions is within the interval of $(-2, +4)$ dB. For typical FBG spectral peak shapes, cumulative standard deviation values along all wavelength positions are shown in green/red/blue, respectively. Values clearly indicate that the DDST detection significantly denoises and smoothes noisy shapes of FBG spectral peaks. The more the FBG spectral peak is noisy, the higher DDST detection efficiency is achieved. For example, in case where the fiber attenuation was 45 dB, a 3.5-fold improvement of stdev@45 dB was achieved.

These improvements in FBG spectral peaks denoising leads to more reliable wavelength measurements, better FBG spectral peak recognition and more precise FBG wavelength shift estimation, especially in systems with high spectral utiliza-
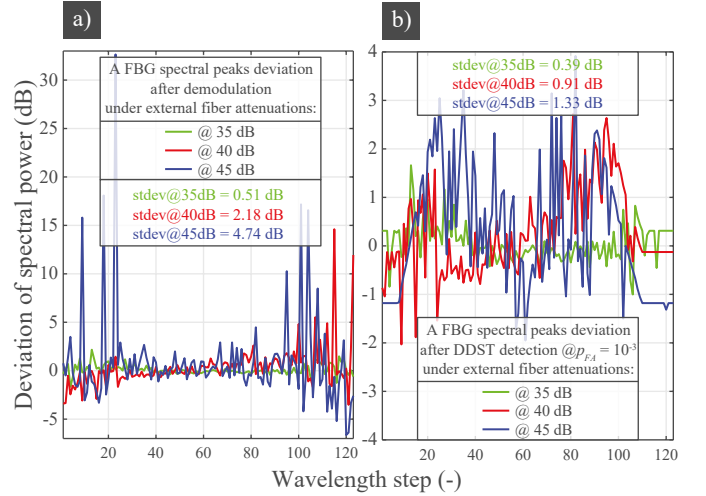

Fig. 18. Comparison of absolute and cumulative standard deviations for FBG spectral peak shapes under 20, 35, 40 and 45 dB fiber attenuation (referenced to cases with 20 dB attenuation): a) after demodulation, b) after DDST detection at $p_{FA} = 10^{-3}$.

tion [25]. We believe that, the DDST detection algorithm can be also used in Rayleigh, Brillouin or even Raman scattering measurement techniques for long-distance sensing like in railway [34] or traffic applications where the background noise and SNR rapidly changes. Since the Brillouin optical time domain reflectometry sensing suffers from low SNR, our approach becomes a good candidate for the future challenges [36], by improving the thresholding in the detection technique.

V. CONCLUSION

In conclusion, a novel algorithm for use in Single Mode Fiber (SMF) sensing applications to determine a Denoising Dynamic Statistical Threshold (DDST) is proposed and demonstrated. The algorithm is capable of effective detection of FBG spectral peaks and their changing spectral location.

The DDST detection algorithm is also capable to detect FBG spectral peaks at the presence of changing SNR. Based on the background noise statistics, this simple but effective algorithm is able to automatically and accurately detect narrow wavelength windows around FBG resonant peaks, by implementing so called spectral windowing. This windowing helps with tracking of FBG spectral peaks, especially in a densely populated FBG sensor networks. Based on SNR (via targeted probability of false alarms, p_{FA}), the full DDST algorithm is able to automatically adapt the detection threshold τ to the fluctuating background noise. At the same time, it preserves the shape of the FBG spectral peaks and improves the post-detection SNR even when the background noise suddenly increases. The full DDST detection algorithm is independent of FBG spectral peaks shapes. When the adjacent FBG spectral peaks overlap partially, it provides a high degree of certainty in rejecting false FBG detection which is important when wavelength overlap rate is higher than 40 %. In a noisy and low SNR environment, the novel DDST detection algorithm provides a highly efficient denoising and smoothing of noisy FBG spectral peaks. We have shown that 3.5-fold improvement of the standard deviation can be achieved under 45 dB fiber attenuation.

REFERENCES

[1] K. Hill and G. Meltz, "Fiber Bragg grating technology fundamentals and overview," *Journal of Lightwave Technology*, vol. 15, no. 8, pp. 1263–1276, 1997. [Online]. Available: http://ieeexplore.ieee.org/document/618320/

[2] T. Erdogan, "Fiber grating spectra," *Journal of Lightwave Technology*, vol. 15, no. 8, pp. 1277–1294, 1997. [Online]. Available: http://ieeexplore.ieee.org/document/618322/

[3] A. Kersey, M. Davis, H. Patrick, M. LeBlanc, K. Koo, C. Askins, M. Putnam, and E. Friebele, "Fiber grating sensors," *Journal of Lightwave Technology*, vol. 15, no. 8, pp. 1442–1463, 1997. [Online]. Available: http://ieeexplore.ieee.org/document/618377/

[4] C. Campanella, A. Cuccovillo, C. Campanella, A. Yurt, and V. Passaro, "Fibre Bragg Grating Based Strain Sensors: Review of Technology and Applications," *Sensors*, vol. 18, no. 9, p. 3115, sep 2018. [Online]. Available: http://www.mdpi.com/1424-8220/18/9/3115

[5] I. R. Matias, S. Ikezawa, and J. Corres, Eds., *Fiber Optic Sensors*, ser. Smart Sensors, Measurement and Instrumentation. Cham: Springer International Publishing, 2017, vol. 21. [Online]. Available: http://link.springer.com/10.1007/978-3-319-42625-9

[6] D. Tosi, "Review and Analysis of Peak Tracking Techniques for Fiber Bragg Grating Sensors," *Sensors*, vol. 17, no. 10, p. 2368, oct 2017. [Online]. Available: http://www.mdpi.com/1424-8220/17/10/2368

[7] Y. Chen, K. Yang, and H.-L. Liu, "Self-Adaptive Multi-Peak Detection Algorithm for FBG Sensing Signal," *IEEE Sensors Journal*, vol. 16, no. 8, pp. 2658–2665, apr 2016. [Online]. Available: https://ieeexplore.ieee.org/document/7378832/

[8] S. Kumar and S. Sengupta, "Efficient detection of multiple FBG wavelength peaks using matched filtering technique," *Optical and Quantum Electronics*, vol. 54, no. 2, p. 89, feb 2022. [Online]. Available: https://link.springer.com/10.1007/s11082-021-03460-3

[9] Y. Zheng, H. Yu, H. Guo, X. Li, and D. Jiang, "Analysis of the Spectrum Distortions of Weak Fiber Bragg Gratings Fabricated In-Line on a Draw Tower by the Phase Mask Technique," *Journal of Lightwave Technology*, vol. 33, no. 12, pp. 2670–2673, jun 2015. [Online]. Available: http://ieeexplore.ieee.org/document/6991515/

[10] Y. Guo, C. Yu, Y. Ni, and H. Wu, "Accurate demodulation algorithm for multi-peak FBG sensor based on invariant moments retrieval," *Optical Fiber Technology*, vol. 54, p. 102129, jan 2020. [Online]. Available: https://linkinghub.elsevier.com/retrieve/pii/S1068520019306546

[11] H. Li, K. Li, H. Li, F. Meng, X. Lou, and L. Zhu, "Recognition and classification of FBG reflection spectrum under non-uniform field based on support vector machine," *Optical Fiber Technology*, vol. 60, p. 102371, dec 2020. [Online]. Available: https://linkinghub.elsevier.com/retrieve/pii/S1068520020303618

[12] Hao Jiang, Jing Chen, and Tundong Liu, "Wavelength Detection in Spectrally Overlapped FBG Sensor Network Using Extreme Learning Machine," *IEEE Photonics Technology Letters*, vol. 26, no. 20, pp. 2031–2034, oct 2014. [Online]. Available: https://ieeexplore.ieee.org/document/6871342

[13] Z. Lv, Y. Wu, W. Zhuang, X. Zhang, and L. Zhu, "A multi-peak detection algorithm for FBG based on WPD-HT," *Optical Fiber Technology*, vol. 68, p. 102805, jan 2022. [Online]. Available: https://linkinghub.elsevier.com/retrieve/pii/S1068520021003552

[14] Z. Cao, S. Zhang, T. Xia, Z. Liu, and Z. Li, "Spectral Demodulation of Fiber Bragg Grating Sensor Based on Deep Convolutional Neural Networks," *Journal of Lightwave Technology*, vol. 40, no. 13, pp. 4429–4435, jul 2022. [Online]. Available: https://ieeexplore.ieee.org/document/9723626/

[15] H. Meikle, *Modern radar systems*, 2nd ed., ser. Artech House radar library. Boston: Artech House, 2008.

[16] G. Cibira, "Envelope and square-law channels fusion," in *2012 13th International Radar Symposium*. IEEE, may 2012, pp. 406–410. [Online]. Available: http://ieeexplore.ieee.org/document/6233355/

[17] G. Cibira, "Inter-channel CFAR detector," in *2012 ELEKTRO*. IEEE, may 2012, pp. 36–41. [Online]. Available: http://ieeexplore.ieee.org/document/6225604/

[18] Yonghong Zeng and Ying-Chang Liang, "Spectrum-Sensing Algorithms for Cognitive Radio Based on Statistical Covariances," *IEEE Transactions on Vehicular Technology*, vol. 58, no. 4, pp. 1804–1815, may 2009. [Online]. Available: http://ieeexplore.ieee.org/document/4610972/

[19] K. Khosravi, H. Shahabi, B. T. Pham, J. Adamowski, A. Shirzadi, B. Pradhan, J. Dou, H.-B. Ly, G. Gróf, H. L. Ho, H. Hong, K. Chapi, and I. Prakash, "A comparative assessment of flood susceptibility modeling using Multi-Criteria Decision-Making Analysis and Machine Learning Methods," *Journal of Hydrology*, vol. 573, pp. 311–323, jun 2019. [Online]. Available: https://linkinghub.elsevier.com/retrieve/pii/S0022169419303026

[20] B. Adebisi, K. Anoh, K. M. Rabie, A. Ikpehai, M. Fernando, and A. Wells, "A New Approach to Peak Threshold Estimation for Impulsive Noise Reduction Over Power Line Fading Channels," *IEEE Systems Journal*, vol. 13, no. 2, pp. 1682–1693, jun 2019. [Online]. Available: https://ieeexplore.ieee.org/document/8327812/

[21] T. Griffith, S.-A. Baker, and N. F. Lepora, "The statistics of optimal decision making: Exploring the relationship between signal detection theory and sequential analysis," *Journal of Mathematical Psychology*, vol. 103, p. 102544, aug 2021. [Online]. Available: https://linkinghub.elsevier.com/retrieve/pii/S002224962100033X

[22] "IEEE Communications Society Integrated Sensing and Communication Emerging Technology Initiative – Integrated Sensing and Communication Emerging Technology Initiative." [Online]. Available: https://isac.committees.comsoc.org/

[23] K. A. Memon, K. H. Mohammadani, A. A. Laghari, R. Yadav, B. Das, W. U. Khan Tareen, N. u. A. Memon, and X. Xin, "Dynamic bandwidth allocation algorithm with demand forecasting mechanism for bandwidth allocations in 10-gigabit-capable passive optical network," *Optik*, vol. 183, pp. 1032–1042, apr 2019. [Online]. Available: https://linkinghub.elsevier.com/retrieve/pii/S0030402619302797

[24] R. A. Butt, M. Faheem, and M. W. Ashraf, "Efficient upstream bandwidth utilization with minimum bandwidth waste for time and wavelength division passive optical network," *Optical and Quantum Electronics*, vol. 52, no. 1, p. 14, jan 2020. [Online]. Available: http://link.springer.com/10.1007/s11082-019-2127-y

[25] G. Cibira, I. Glesk, and J. Dubovan, "Dynamic Bandwidth Allocation for C-Band Shared FBG Sensing and Telecommunications," *IEEE Internet of Things Journal*, vol. 9, no. 22, pp. 23 272–23 284, nov 2022. [Online]. Available: https://ieeexplore.ieee.org/document/9815049/

[26] "Sensing systems." [Online]. Available: https://www.sylex.sk/products/sensing-systems/

[27] X. Guo, "Research on Peak-Detection Algorithms of Fiber Bragg Grating Demodulation," 2022, pp. 112–122. [Online]. Available: https://link.springer.com/10.1007/978-981-16-5692-7_12

[28] N. L. Johnson, S. Kotz, and N. Balakrishnan, *Continuous univariate distributions*, 2nd ed., ser. Wiley series in probability and mathematical statistics. New York: Wiley, 1994.

[29] J. Jacod and P. Protter, *Probability Essentials*, ser. Universitext. Berlin, Heidelberg: Springer Berlin Heidelberg, 2004. [Online]. Available: http://link.springer.com/10.1007/978-3-642-55682-1

[30] "ITU-T G.652: Characteristics of a single-mode optical fibre and cable." [Online]. Available: https://www.itu.int/rec/T-REC-G.652-201611-I/en

[31] Y. Chen, Z. Liu, and H. Liu, "A Method of Fiber Bragg Grating Sensing Signal De-Noise Based on Compressive Sensing,"

IEEE Access, vol. 6, pp. 28 318–28 327, 2018. [Online]. Available: https://ieeexplore.ieee.org/document/8325457/

[32] D. J. Spiegelhalter, N. G. Best, B. P. Carlin, and A. van der Linde, "Bayesian measures of model complexity and fit," *Journal of the Royal Statistical Society: Series B (Statistical Methodology)*, vol. 64, no. 4, pp. 583–639, oct 2002. [Online]. Available: https://onlinelibrary.wiley.com/doi/10.1111/1467-9868.00353

[33] A. Jones, *Probability, statistics and other frightening stuff*, ser. Working guides to estimating and forecasting. Abingdon, Oxon ; New York, NY: Routledge, 2018.

[34] C. Du, S. Dutta, P. Kurup, T. Yu, and X. Wang, "A review of railway infrastructure monitoring using fiber optic sensors," *Sensors and Actuators A: Physical*, vol. 303, p. 111728, mar 2020. [Online]. Available: https://linkinghub.elsevier.com/retrieve/pii/S0924424719309483

[35] A. C. L. Wong and G.-D. Peng, "Applications of Discrete Wavelet Transform in Optical Fibre Sensing," in *Discrete Wavelet Transforms - Biomedical Applications*. InTech, sep 2011. [Online]. Available: http://www.intechopen.com/books/discrete-wavelet-transforms-biomedical-applications/applications-of-discrete-wavelet-transform-in-optical-fibre-sensing

[36] Q. Bai, Q. Wang, D. Wang, Y. Wang, Y. Gao, H. Zhang, M. Zhang, and B. Jin, "Recent Advances in Brillouin Optical Time Domain Reflectometry," *Sensors*, vol. 19, no. 8, p. 1862, apr 2019. [Online]. Available: https://www.mdpi.com/1424-8220/19/8/1862